# Optimization of energy transport in the Fenna-Matthews-Olson complex via sitevarying pigment-protein interactions

Cite as: J. Chem. Phys. **150**, 085102 (2019); https://doi.org/10.1063/1.5048058 Submitted: 11 July 2018 . Accepted: 01 February 2019 . Published Online: 26 February 2019

S. A. Oh, D. F. Coker (10), and D. A. W. Hutchinson







#### ARTICLES YOU MAY BE INTERESTED IN

Environment-assisted quantum walks in photosynthetic energy transfer
The Journal of Chemical Physics 129, 174106 (2008); https://doi.org/10.1063/1.3002335

Quantumness in light harvesting is determined by vibrational dynamics
The Journal of Chemical Physics 149, 234102 (2018); https://doi.org/10.1063/1.5058136

Unified treatment of quantum coherent and incoherent hopping dynamics in electronic energy transfer: Reduced hierarchy equation approach

The Journal of Chemical Physics 130, 234111 (2009); https://doi.org/10.1063/1.3155372





## **Optimization of energy transport** in the Fenna-Matthews-Olson complex via site-varying pigment-protein interactions

Cite as: J. Chem. Phys. 150, 085102 (2019); doi: 10.1063/1.5048058

Submitted: 11 July 2018 • Accepted: 1 February 2019 •

Published Online: 26 February 2019







S. A. Oh. D. F. Coker. 2,a) and D. A. W. Hutchinson 1,3,b)



#### **AFFILIATIONS**

- Dodd-Walls Centre for Photonic and Quantum Technologies, Department of Physics, University of Otago, Dunedin 9016, New Zealand
- <sup>2</sup>Department of Chemistry, Boston University, Boston, Massachusetts 02215, USA
- Centre for Quantum Technologies, National University of Singapore, 3 Science Drive 2, Singapore 117543, Singapore
- a) Electronic mail: coker@bu.edu
- b) Electronic mail: david.hutchinson@otago.ac.nz

#### **ABSTRACT**

Energy transport in photosynthetic systems can be tremendously efficient. In particular, we study exciton transport in the Fenna-Mathews-Olson (FMO) complex found in green sulphur bacteria. The exciton dynamics and energy transfer efficiency depend on the interaction of excited chromophores with their environment. Based upon realistic, site-dependent models of the systembath coupling, we present results that suggest that this interaction may be optimized in the case of FMO. Furthermore we verify two transport pathways and note that one is dominated by coherent dynamics and the other by incoherent energy dissipation. In particular, we note a significant correlation between energy transport efficiency and coherence for exciton transfer from bacteriochlorophyll (BChl) 8 to BChl 4.

Published under license by AIP Publishing. https://doi.org/10.1063/1.5048058

#### I. INTRODUCTION

Despite the importance of the effect of the environment upon energy transport in photosynthetic systems, it is common practice in theoretical studies to assume that the local environments of different chromophores are similar and to assign identical spectral densities describing the interaction of the excited molecules with their nuclear vibrational environments. While this simplistic approach should still allow the essential physics to be captured, it may nevertheless mask the influence of realistic site variations which could potentially contain interesting physics.

Recent computational chemistry calculations have shown, for instance, in the case of the Fenna-Matthews-Olson (FMO) complex of the green sulfur bacteria, that site variations of spectral density can be significant.<sup>1-3</sup> Obviously, in biological systems, traits showing some degree of heterogeneity are expected, and in many cases, they are simply random.

However, the green sulfur bacteria, due to its ability to survive under extremely low-light conditions, must certainly possess highly evolved light-harvesting machinery. It is then only natural to suspect that there may be an underlying design principle associated with these heterogeneous system-bath couplings. A previous publication demonstrated that the heterogeneous spectral densities can significantly impact exciton transport dynamics and suggested that this could be a mechanism used to tune energy transport.2 In addition, exciton delocalization may also be affected by site-dependent system-bath couplings.

It has been found, for example,4 that the duration and robustness of quantum beats in site populations in a generic dimer (a signature of quantum coherence) are simultaneously increased under conditions with specific ratios of site energy mismatch to site reorganization energy mismatch. The results of 2D electronic spectroscopy (2DES) experiments show coherent quantum beats persisting over the time scale

of exciton dynamics. It has been speculated that this quantum coherent character of the dynamics may enable quantum walks that can simultaneously sample multiple energy transfer pathways and this, in part, contributes to the high efficiency of photosynthetic energy transport. Regardless of its actual role, the observed coherent evolution underlying energy transport in light-harvesting complexes must be accounted for in theoretical studies of their dynamics. Some studies, albeit based on approximate perturbative methods, suggest that optimal transport occurs in the intermediate regime between the coherent and incoherent limits.5-10 However, it remains an open question whether or not, in this optimal regime, comparable or even better efficiency might be achieved by a more classical type of mechanism, e.g., energy funneling. As such, it is entirely plausible that the presence of quantum coherence may simply be a by-product of dense chromophore packing, with no specific function of its own. Finding evidence of underlying coherence optimization and a system design that can effectively utilize coherence, however, would help to address this important mechanistic question, particularly in the context of energy transport efficiency.

In this work, we present some results that suggest that the site-varying spectral densities of the FMO complex may be partially optimized for enhanced energy transport. This finding has been made possible by the availability of accurate site-dependent spectral densities from recent quantum chemistry/molecular dynamics calculations.<sup>1,11</sup>

The basic theories of energy transport or spectroscopic response assume that the full Hamiltonian can be broken into a system part,  $\hat{H}_s$ , a bath, or environmental component,  $\hat{H}_b$ , and an interaction between these system and bath subsystems,  $\hat{H}_{sb}$ . The partitioning of the different degrees of freedom between the system and bath subsystems is determined by the resolution capabilities of a given experiment. Thus, for example, high resolution 2D electronic spectroscopy (2DES) can actually resolve transitions between higher frequency intramolecular vibrational and electronic states, so in such experiments the system part is well described by the vibronic eigenstates of the chromophores and the bath becomes the lower frequency environmental, or intermolecular degrees of freedom. For less well resolved experiments, for example, monitoring energy migration from one chromophore to another and not resolving (i.e., averaging over) the intramolecular vibrational structure of the chromophores, the system is well described by the coupled chromophore electronic states, while the bath becomes all the intra- and intermolecular vibrations. The study presented here approximately adopts this latter perspective in that it assumes that  $\hat{H}_s$  is represented by the eigenstates of the coupled electronic subsystem, while the intermolecular spectral density composed of a continuum of protein environmental modes describes the bath. In these studies, we will disregard the influence of the discrete intramolecular component of the spectral density as they are expected to play a fairly minor role in energy transport in chlorophyll systems with small intramolecular Huang-Rhys factors. There is the possibility of further optimization from vibronic contribution and interplay with the intermolecular component of the spectral density; however, preliminary results from studies of these effects suggest that their inclusion does not materially affect the conclusions based on the results we presented here.<sup>12</sup>

#### **II. THEORETICAL MODEL**

The total system-bath Hamiltonian is expressed as

$$\hat{H}_{tot} = \hat{H}_s + \hat{H}_b + \hat{H}_{sb},\tag{1}$$

where  $\hat{H}_s$ ,  $\hat{H}_b$ , and  $\hat{H}_{sb}$  are the system (electronic), bath, and system-bath interaction Hamiltonians, respectively.

#### A. The electronic system

The electronic system consists of the chromophores in the pigment-protein complex (PPC). Its Hamiltonian governs the coherent part of the evolution and is described by the tight-binding model in the site basis states,  $|m\rangle$ ,

$$\hat{H}_{s} = \sum_{m=1}^{N} E_{m} |m\rangle\langle m| + \sum_{m\neq n}^{N} V_{mn} |m\rangle\langle n|, \qquad (2)$$

where  $E_m$ ,  $V_{mn}$ , and N are the site energies, the electronic coupling between pigments m and n, and the number of chromophores, respectively. Since the PPC operates under low light conditions, the single exciton manifold approximation is valid. The  $\alpha$ th eigenstate of the system Hamiltonian (also known as an exciton state) can be decomposed in terms of the site basis states as

$$|\alpha\rangle = \sum_{m} c_{m,\alpha} |m\rangle.$$
 (3)

Throughout we will employ latin labels for the exciton basis states. In this work, we use the 8-site Hamiltonian for the Prosthecochloris aestuarii (P. aestuarii) species, as presented by Moix et al.<sup>13</sup>

#### B. The bath and system-bath coupling

The protein environment is commonly modelled as a bath of harmonic oscillators with  $\hat{H}_b = \sum\limits_{i,m} \left(\hbar\omega_{i,m}b_{i,m}^{\dagger}b_{i,m} + \frac{1}{2}\right)_m$ , where

 $b_{i,m}^{\dagger}(b_{i,m})$  are the creation (annihilation) operators of excitations of the ith bath mode with frequency  $\omega_{i,m}$  on pigment m. In this work, the phonon modes on each site are treated as being uncorrelated and are assumed to be coupled linearly to the populations of the sites in the system Hamiltonian such that

$$\hat{H}_{sb} = \sum_{i,m} u_{i,m} (b_{i,m}^{\dagger} + b_{i,m}) |m\rangle\langle m|. \tag{4}$$

Here  $u_{i,m}$  is the strength of the coupling between the electronic transition of the mth site and the ith phonon mode. Physically, this equation reflects the effect of the protein environment dynamically modulating the site energies of the pigments. All information about the system-bath interaction of each pigment m is contained in its corresponding spectral

density  $J_m(\omega) = \pi \sum_i |u_{i,m}|^2 \delta(\omega - \omega_{i,m})$ . The total reorganization energy,  $\lambda_m = \sum_i |u_{i,m}|^2 / \omega_{i,m}$ , of pigment m is made up of contributions from each mode, i, and is related to  $J_m(\omega)$  by the following integration over the bath frequencies  $\omega$ :

$$\lambda_m = \frac{1}{\pi} \int_0^\infty \frac{J_m(\omega)}{\omega} d\omega. \tag{5}$$

#### **III. NUMERICAL METHODS**

The numerical computation of the dynamics was performed using the Modified Redfield Theory (MRT)<sup>14</sup> and its more recent upgrade, the Coherent Modified Redfield Theory (CMRT).<sup>15–18</sup> Despite being perturbative, approximate methods, it has been shown that MRT and CMRT can be reliable over a fairly broad range of system-bath coupling strengths and provide reasonable agreement with dynamics computed from numerically exact methods.<sup>15,17,19</sup> This is particularly true for the relatively weak range of system-bath coupling strengths that are found in the FMO complex we explore, making these methods a good choice for the studies reported here. This, coupled with the convenience and efficiency as compared to numerically exact methods, makes them suitable numerical methods for this work.

In contrast to MRT, CMRT allows the computation of coherence terms in the density matrix as well as the incorporation of some non-Markovianity. In addition, while the MRT population vector P(t) is only provided in the exciton basis due to limitations in the formulation of this approach, the CMRT density matrix  $\rho(t)$  can be obtained in both the site and exciton basis (Appendix C). The downside of CMRT, however, and the reason why both versions of this approach were employed in our studies, is its much longer computation time. This renders the use of CMRT infeasible for the statistical methods and genetic algorithm used in Secs. V A and V B, respectively, which require only the population terms. We thus employ MRT in these cases while using CMRT for the rest of the work in this paper, in particular, providing benchmarks for our MRT simulations. As in Refs. 17 and 18, we solve for the non-Markovian dynamics of CMRT with the non-Markovian Quantum Jump (NMQJ) technique.20,21

To justify the use of MRT in place of CMRT, we have checked that the effects of non-Markovianity are not overly significant, or in other words, the general trend of population dynamics (in the exciton basis) is similar with the two versions. For completeness, we give a brief outline of MRT, CMRT, and NMQJ in Appendixes A, B, and C, respectively. The full derivation and additional details can be found in Refs. 14 and 19 for MRT, Refs. 15–18 for CMRT, and Refs. 20 and 21 for NMQJ. All energy transfer efficiency computations were performed for the physiological temperature of T = 300 K.

#### IV. NUMERICAL SETUP

The two most important pigments for our analysis of the FMO complex are the initial excitation site and the target site—the former influences the exciton dynamics and the latter determines our assessment of energy transport efficiency.

It is now believed that bacteriochlorophyll (BChl) 8 is the most likely linker site between the chlorosome and the rest of the FMO complex.<sup>22</sup> However, BChl 8 is normally lost during sample preparation, and before its recent discovery,<sup>23,24</sup> BChls 1 and 6 were proposed as the possible linker sites. These two pigments are also the usual initial photoexcitation sites in spectroscopic experiments. For these reasons, many theoretical studies employ BChls 1 and 6 as the initial excitation sites. Since our motivation is to understand the *in vivo* workings of the FMO complex and not for comparison to spectroscopic data, we choose BChl 8 as our initial excitation site for this work.

In the literature, the linker site to the reaction centre is usually assumed to be BChl 3, which is also the lowest energy pigment with the closest proximity to the reaction centre. There exists some ambiguity, however. Wen et al.<sup>25</sup> reported that it is the BChl 3 site of the FMO complex that interacts with the reaction centre, but their experiments did not pinpoint the exact pigment(s). Furthermore, it has been mentioned in several publications<sup>7,26-30</sup> that the two lowest energy pigments, BChls 3 and 4, are in the target region close to, or in contact with the reaction centre. As such, we consider both BChls 3 and 4 as the possible target sites in this paper.

To aid physical interpretation, we represent the realistic spectral densities in the Drude-Lorentz regularized Ohmic form<sup>31</sup>

$$J_m^{DL}(\omega) = 2\lambda_m \Omega_m \frac{\omega}{\omega^2 + \Omega_m^2},$$
 (6)

where  $\lambda_m$  and  $\Omega_m$  are the reorganization energy and cutoff frequency of site m, respectively. Here the values of  $\lambda_m$  are calculated from the realistic site spectral densities² using Eq. (5). The cutoff frequency,  $\Omega_m$ , which corresponds to the inverse of the bath correlation time, can be obtained by first computing the site-dependent bath correlation function [Eq. (A6)]. For simplicity, we assume that the real part of the bath correlation functions can be represented by time decaying exponential functions, from which it is possible to extract the bath correlation time and subsequently  $\Omega_m$ . We have verified that the dynamics with the realistic site-dependent spectral densities can be reliably reproduced with their Drude-Lorentz forms.

The computed values of  $\lambda_m$  and  $\Omega_m$  are presented in Table I. It is clear that the FMO complex has a fairly significant range of  $\lambda_m$  values where the largest is more than 2.5 times the magnitude of the smallest. It is interesting to note that the mean reorganization energy is also in the sense the most representative since half of the pigments have  $\lambda_m$  values close to this value.

The complexity of the problem is now significantly reduced since the spectral densities are characterized by only two physically meaningful bath parameters, i.e.,  $\lambda_m$  and  $\Omega_m$ . It turns out that the problem can be further simplified. By comparing the dynamics obtained with site variation in only one of the bath parameters to that obtained with a completely site-independent benchmark, we established that it is primarily the site variation in  $\lambda_m$  which modifies the dynamics, with

**TABLE I.** Site-dependent reorganization energies  $\lambda_m$  and cutoff frequencies  $\Omega_m$  of the FMO Drude-Lorentz spectral density used in this work.

m	$\lambda_m  (\mathrm{cm}^{-1})$	$\Omega_m$ (cm <sup>-1</sup> )
1	21.28	40.96
2	31.52	88.04
3	22.86	43.52
4	17.88	48.79
5	15.36	52.10
6	23.18	43.55
7	24.89	39.35
8	41.00	37.31
Mean	24.75	49.20

very little contribution from the  $\Omega_m$  site variation. Here the site-independent case is constructed by assigning the mean value of  $\lambda_m$  and/or  $\Omega_m$  from Table I. Importantly, we note an improvement in exciton transport to the target sites with the site-varying spectral density.

Therefore, all computations exploring the influence of site-dependent spectral densities on energy transfer efficiency have been performed using the Drude-Lorentz spectral density representation, keeping the site-dependent  $\Omega_m$  fixed to the original configuration values in Table I and varying only  $\lambda_m$ .

#### V. RESULTS

The focus of the results reported here is on how sitedependent spectral densities might influence energy transfer efficiency. Systematic measurements of various quantities that influence energy transfer efficiency of small molecular aggregates like the FMO complex are not easily available from simple experiments so our approach proceeds by comparing computed results that use models with explicit computed site-dependent spectral densities versus results from averaged, site-independent models. To make a solid connection between this model exploration of energy transfer and real experimental results in Appendix G, we demonstrate that the site-dependent spectral density variability is expected to have an influence on real measurable quantities. In Appendix G, for example, we show that the predicted variability of the sitedependent spectral densities can sharpen up some features in the spectra, relative to others, and enhance agreement with experimental results. The fact that these enhancements are fairly modest may be due to the use of various adjustable parameters in the model that compensate to give an overall best fit. Nevertheless, despite the modest enhancement in agreement for absorption and circular dichroism (CD) signals obtained with computed site-dependent spectral densities reported in Appendix G, we find that this is correlated with significant enhancement in energy transfer efficiency that seems to be robust to the choice of model. In Secs. V A-V C, we detail our energy transfer efficiency measure and explore factors affecting optimality for different energy transfer pathways.

## A. Optimality of the system-bath coupling configuration

To quantify the influence of site-dependent spectral density on energy transport enhancement, a rigorous assessment of optimality is necessary. To this end, the relative energy transfer efficiency with the FMO site-dependent  $\lambda_m$  configuration must be compared with that from a large sample of random site-dependent  $\lambda_m$  configurations. Silbey and coworkers<sup>32</sup> have presented a simple kinetic theory for the efficiency of a light harvesting network based on residence times of the network sites, and relative rate constants for either trapping at a site or losing excitation energy from the network by, e.g., radiative or other decay processes from each site. The efficiency is then determined as the ratio of the probability that the excitation remains in the network (sum of the products of residence times × trapping rates) divided by a similar quantity for all processes, i.e., both trapping in the network and decay or loss from the network. To simplify our calculations, we adopt a widely used proxy for network efficiency.33-37 As mentioned above, for speed of computation and sampling the dynamics of many representative model spectral densities, we employ MRT for our treatment of exciton network dynamics. This approach evolves only exciton populations and because we do not have the available off-diagonal coherence elements of the density matrix with this approach, we cannot transform between exciton and site representations. Our proxy for energy transfer efficiency is based on the idea that the faster the excitation energy moves through the network to the localized target state, the less time there is for decay from intermediate chromophores and thus loss of energy from within the network. Our measure of efficiency then involves choosing an appropriate time-averaging interval and is based on the time-averaged population in the exciton state that is dominated by the pre-selected target site basis state. Thus our proxy for relative energy transfer efficiency, as obtained using the MRT formulation, is

$$\zeta_m = \frac{1}{\tau} \int_0^\tau P_{\alpha}(t) dt$$
, where  $|c_{m,\alpha}|^2$  is maximal. (7)

Here  $P_{\alpha}$  is the population in the exciton state  $\alpha$ , with  $\alpha = 1(2)$ , for the target site m = 3(4). The participation of an exciton state in each site is denoted by the absolute square of the corresponding expansion coefficient in Eq. (3) and ranges from 0 to 1. For the two target sites, we consider (3 and 4) and we find that  $|c_{3,1}|^2 = 0.88$  and  $|c_{4,2}|^2 = 0.59$ . We have chosen  $\tau$  = 1 ps since a large portion of the relevant exciton dynamics and the experimentally observed coherence occur within this time scale. As we can see, a higher value of  $\zeta_m$  reflects a higher population transfer rate to the chosen target state. Obviously, unlike the % efficiency figure of merit,  $\zeta_m$  does not provide an intuitive gauge of efficiency when considered in isolation. Nevertheless, it is still useful for comparative purposes, which is sufficient for the study we described here. In addition, based on existing knowledge of photosynthetic lightharvesting efficiency, we would expect the  $\zeta_m$  value for at least the realistic  $\lambda_m$  configuration to correspond to a near 100% efficiency.

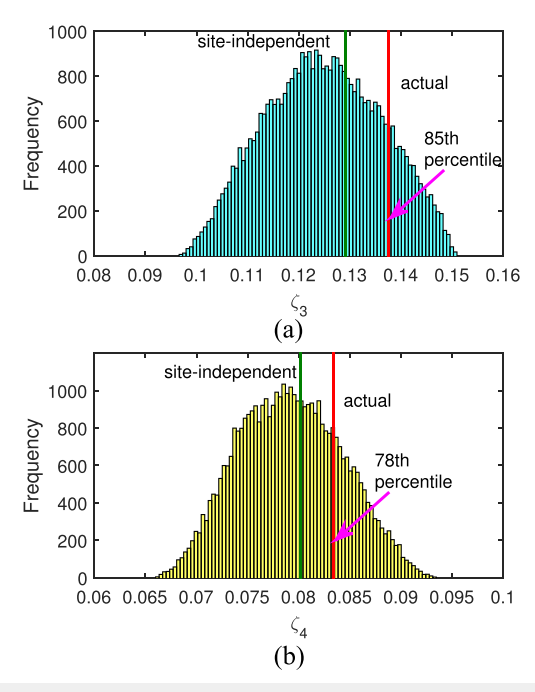


**FIG. 1.** Histogram of efficiencies  $\zeta_m$  for all possible site permutations of  $\lambda_m$  for the exciton state (corresponding target site) of (a)  $\alpha$  = 1 (BChI 3) and (b)  $\alpha$  = 2 (BChI 4). In both histograms, the original configuration is also included in the sample. The red and green vertical lines indicate the position on the histogram of the original and site-independent configurations, respectively. Numerical method: MRT

Two types of randomizations were performed. In the first set, the relative efficiency, as determined by their  $\zeta_m$  values, of all possible site permutations of the original  $\lambda_m$  configuration was computed and presented as a histogram in Fig. 1. Notice that the efficiency of the actual FMO  $\lambda_m$  configuration falls significantly in the upper percentile range (85th and 78th percentile for the target sites of BChls 3 and 4, respectively). The fact that it is not the most efficient configuration is not a concern here. In fact, it is not surprising in the context of evolution since biological constraints may be present and traits only need to be sufficiently functional. In contrast, the site-independent case yields an efficiency closer to the mode of the distribution. A similarly high level of optimization is also observed in our second set of randomization, where now the only constraints on the values are that the mean, maximum, and minimum of each set of sampled  $\lambda_m$  values are similar to those of the original configuration. For consistency, the same sample size as the first set, i.e., 40 320 was used. As shown in Fig. 5 of Appendix E, the efficiency corresponding to the original  $\lambda_m$  configuration is in the 87th and 81st percentile for the target sites of BChls 3 and 4, respectively, with this alternative randomization approach. Once again, the efficiency for the site-independent case appears near the mode of the distribution. To provide a visualization of how a random unoptimized  $\lambda_m$  configuration could be detrimental to transport efficiency, we present in Fig. 2 a comparison of the exciton dynamics with the original  $\lambda_m$ 

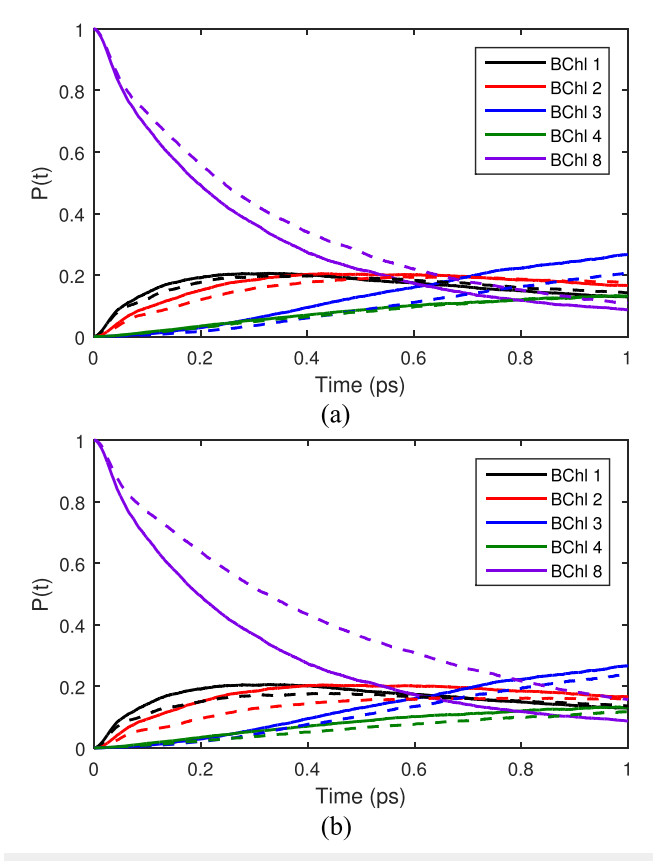


**FIG. 2**. Site population dynamics showing the disparity in energy transport performance with the original FMO  $\lambda_m$  configuration (solid curves) and the least efficient site permutation of  $\lambda_m$  (dashed curves) for the target site of (a) BChl 3 and (b) BChl 4. Numerical method: CMRT.

configuration to that with the least efficient configuration in Fig. 1.

Finally, it is worth mentioning that when we tested BChls 1 and 6 as the initial excitation sites, no such optimization is present. Compared to the site-independent case, there is no appreciable improvement in energy transport in the case of BChl 1, while for BChl 6, there is in fact a deterioration in efficiency. Assuming the distribution of  $\lambda_m$  is a result of evolution to optimize energy transport, this observation is further testament that BChl 8 is likely the first pigment to receive the exciton from the chlorosome.

#### **B.** Source of optimality

Having established that the actual site-dependent  $\lambda_m$  configuration is significantly optimized for energy transport to both BChls 3 and 4, we seek to identify the underlying mechanism behind its effectiveness. We note that network connectivity and site energy distribution determine how effective a particular mode of energy transport (dissipative or coherent) will be. Moreover, larger reorganization energies are conducive to energy dissipation, while smaller

reorganization energies are beneficial for sustaining quantum coherence. This suggests an optimized interplay between the FMO  $\lambda_m$  distribution and the design of the electronic

Therefore, to determine if the system design is optimized for a dissipative or coherent mode of transport, we establish whether the best efficiency is obtained with larger or smaller values of  $\lambda_m$ . This is achieved through the use of a genetic algorithm (Appendix F). Here, the fitness function is the same measure of relative efficiency used in Sec. V A, i.e., the efficiency for transport to the exciton state dominated by the selected target site as evaluated with the MRT formulation [Eq. (7)].

For the BChl 3 target site, the optimal configuration found by the basic genetic algorithm search outlined in Appendix F is one where all the sites have the maximum  $\lambda_m$  value permitted during the search. Clearly, the optimal mechanism of energy transport to this target site must be a dissipative one. On the other hand, for the target site of BChl 4, the optimal  $\lambda_m$  values are found to be minimized for the three lowest energy pigments (BChls 2, 3, and 4) and maximized for the remaining pigments. This suggests that a combined coherent and dissipative mechanism leads to the optimal energy transport in this case. We note that the minimization for BChls 3 and 4 for this target could partly be due to increased coherence prolonging linear combinations between two sites. This would lead to increased population in BChl 4 on average compared to if the process was dissipative, promoting only downhill energy flow to BChl 3. However, we do not see any evidence of Rabi oscillations suggesting that this process is highly overdamped.

Next, we performed a second genetic algorithm search, but this time with a constraint on the mean, mimicking the conditions in Sec. V A. With this constrained genetic search, it is now possible to assess the significance of each pigment to the energy transport process. This is because the only way now for the algorithm to maximize efficiency is through prioritizing the most important pigments by assigning them the best  $\lambda_m$  values and leaving the remainder to the less influential pigments. Thus, in a dissipative process, for example, the more influential a pigment is, the larger the computed optimal  $\lambda_m$  would be.

The results from the second genetic algorithm run are presented in Table II, where the computed optimal values are now labelled  $\lambda_{m,3}^{ga}$  and  $\lambda_{m,4}^{ga}$  for the target sites of BChls 3 and 4, respectively. From the larger values of  $\lambda^{ga}_{m,3}$ , it is clear that the dominant pathway consists of BChls 8, 1, 2, and 3, while BChls 4, 5, 6, and 7 only have minimal contributions. This, together with the previous finding of a dissipative mode of transport, is consistent with the findings of Moix et al. <sup>13</sup> Meanwhile, based on the magnitudes of  $\lambda_{m,4}^{ga}$ , we can infer that the dissipative part of the process predominantly involves BChls 1, 7, and 8,

with less significant contribution from BChls 5 and 6. The  $\lambda^{ga}_{m,3}$  and  $\lambda^{ga}_{m,4}$  configurations also provide useful optimality benchmarks. Through comparison with the FMO  $\lambda_m$  configuration, the source of its high degree of optimality can be identified. With the exception of  $\lambda_1$ , all the site

**TABLE II.** Original site-dependent reorganization energies  $\lambda_m$  of the FMO complex and the optimal configuration of site-dependent reorganization energies  $\lambda_{m,3}^{ga}$  and  $\lambda_{m,4}^{ga}$  as determined by a genetic algorithm for exciton states (corresponding target sites) of  $\alpha$  = 1 (BChl 3) and ( $\alpha$  = 2) (BChl 4), respectively. The mean, lower bound, and upper bound for the solution of the genetic algorithm have been set to be similar to that of the original FMO configuration. Numerical method: MRT.

m	$\lambda_m$ (cm <sup>-1</sup> )	$\lambda_{m,3}^{ga}$ (cm <sup>-1</sup> )	$\lambda_{m,4}^{ga}  (\mathrm{cm}^{-1})$
1	21.28	36.37	40.95
2	31.52	32.44	15.37
3	22.86	40.52	15.36
4	17.88	15.36	15.36
5	15.36	15.36	19.95
6	23.18	15.36	21.27
7	24.89	15.36	37.79
8	41.00	27.21	31.92

reorganization energies show some level of optimization for either one or both of the target sites. The two smallest  $\lambda_m$ values,  $\lambda_4$  and  $\lambda_5$ , show a high degree of agreement with the genetic algorithm values for both target sites.  $\lambda_2$  and  $\lambda_6$  are optimized for only one of the target sites. Meanwhile, the values of  $\lambda_3$  and  $\lambda_7$  are somewhere in between the optimized values for the two target sites, thus achieving a compromise. Finally,  $\lambda_8$ , despite being close to neither of the optimized values, shows a similar trend to the genetic algorithm results by virtue of its larger than average value. With regard to the mutual optimization for both target sites, three mechanisms of optimization can be identified. The first is where the magnitude of  $\lambda_m$  mutually benefits both target sites, for example, the larger than average value of  $\lambda_8$  is advantageous for the dissipative type of energy transport to both BChls 3 and 4. The second mechanism, which is also the most interesting, is where the magnitude of  $\lambda_m$  benefits only one of the target sites, while minimizing its negative effects on the other target site. This applies when a particular pigment is involved in different effective modes of transport to each of the target sites. A case in point is the small value of  $\lambda_4$ , which is advantageous for the partially coherent energy transport to the target site of BChl 4. At the same time, it does not overly impede dissipative energy transport to the target site of BChl 3 since the dominant pathway is not involved. Finally, the third mechanism is one where the magnitude of  $\lambda_m$  does not assist energy transport to any of the target sites, but the negative impact is simply minimized. For example, the small value of  $\lambda_5$  is unfavourable for the dissipative energy transport to both target sites, but the negative effect is mutually minimized since BChl 5 is not on a dominant pathway for any of

At this juncture, we must stress that it is not the  $\lambda_m$  site variation per se that is responsible for the enhanced performance since it is really the magnitude of  $\lambda_m$  that matters. Rather, it is more likely a case of nature making the best of an unavoidable situation. Biological constraints in the FMO can lead to site variation in  $\lambda_m$ ; for example, pigments located at the protein-solvent interface tend to have larger reorganization energies than those in the interior.<sup>2</sup> The high efficiency of the FMO  $\lambda_m$  configuration compared to various other random configurations of similar average (Sec. V A) is then simply a consequence of the system and system-bath interaction having evolved to complement each other in a very effective manner, e.g., via selection of appropriate dominant pathways and effective transport mechanisms.

#### C. Relevance of quantum coherence to efficiency

Given the evidence for both dissipative and coherent energy transport pathways, we investigate how energy transport efficiency relates to the coherence length in the presence of site-dependent  $\lambda_m$ . Since the coherence terms of the density matrix are required, all the computation in this section is performed using the CMRT formulation. For the efficiency  $\eta_m$ , we utilize a measure similar to Eq. (7) but for the site basis counterpart, i.e.,

$$\eta_m = \frac{1}{\tau} \int_0^\tau \rho_{mm}(t) dt, \tag{8}$$

where  $\rho_{mn}(t)$  are the elements of the time-dependent density matrix computed using the CMRT formulation, with the diagonal elements  $\rho_{mm}(t)$  representing the population at site m. Here m=3(4) for the target site of BChl 3 (4). As before, we choose  $\tau=1$  ps.

To quantify the degree of exciton delocalization, we use the coherence length measure,  $L_{\rho}$  defined as the inverse participation ratio treating the absolute value of the time dependent density matrix elements as a distribution function 38,39

$$L_{\rho}(t) = \frac{(\sum_{mn}^{N} |\rho_{mn}(t)|)^{2}}{N \sum_{mn}^{N} |\rho_{mn}(t)|^{2}},$$
(9)

Larger  $L_{\rho}(t)$  values, bounded by the maximum value of N, indicate a larger degree of delocalization. In our calculations, at t=0, the excitation is completely localized at a single site, in which case  $L_{\rho}(0)=1/N$ . As a result,  $L_{\rho}(t)$  starts from 1/N in all cases, increases then peaks after a certain period of time before decreasing towards its thermal equilibrium value. This reflects the scenario of an initially localized pure state becoming more delocalized before the interaction with the environment gradually destroys the coherence. With the original  $\lambda_m$  configuration,  $L_{\rho}(t)$  peaks at the value of about 2 around t=0.7 ps, corresponding to the fact that within the chosen time scale of  $\tau=1$  ps, the dynamics are still relatively far from thermal equilibrium. Note, however, that at finite temperature the state of complete incoherence can never be reached even at equilibrium.

In analogy to Eqs. (7) and (8), we define the time-averaged coherence length as

$$L_{\rho,avg} = \frac{1}{\tau} \int_0^{\tau} L_{\rho}(t) dt.$$
 (10)

The relationship between efficiency  $\eta_m$  and the timeaveraged coherence length  $L_{\rho,avg}$  is depicted as a scatter plot in Fig. 3. The data points correspond to 200 random site-dependent  $\lambda_m$  configuration plus 6 additional relevant data points, namely, the original configuration, the siteindependent configuration, the optimized solution from the

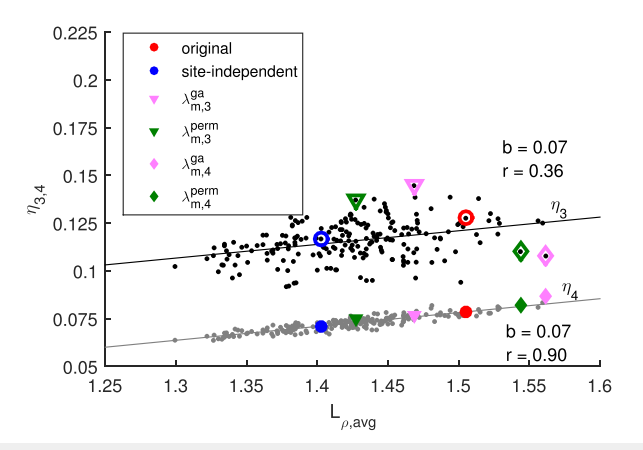


**FIG. 3.** Scatter plot of efficiency  $\eta_m$  as a function of the time-averaged coherence length  $L_{\rho,avg}$  for the assigned target sites of BChls 3 and 4. Black and grey dots represent  $(L_{\rho,avg},\eta_3)$  and  $(L_{\rho,avg},\eta_4)$  data points, respectively, and correspond to 200 random site-dependent  $\lambda_m$  configurations with the same mean, maximum, and minimum as the original. Coloured markers represent data points from the following  $\lambda_m$  configurations: original, site-independent, optimized  $\lambda_m$  configuration from the genetic algorithm (for both target sites BChls 3 and 4) and the most efficient site permutation of original  $\lambda_m$  (for both target sites BChls 3 and 4). Open markers are for  $\eta_3$  while solid markers are for  $\eta_4$ . The linear regression line corresponding to  $\eta_3$  ( $\eta_4$ ) is shown in black (grey). b and r are the slope of the regression line and the correlation coefficient, respectively. Numerical method: CMRT.

genetic algorithm (i.e.,  $\lambda_{m,3}^{ga}$  and  $\lambda_{m,4}^{ga}$ ) and the most efficient site permutation of the original configuration (which we shall denote as  $\lambda_{m,3}^{perm}$  and  $\lambda_{m,4}^{perm}$  for target sites BChls 3 and 4, respectively). For the target site of BChl 3 (Fig. 3), even though there is a positive correlation between  $L_{\rho,avg}$  and  $\eta_m$ , it is in the weak to moderate regime, with a correlation coefficient of only 0.36. This relatively weak correlation implies that it is unlikely that effects due to coherence are significant in the energy transport mechanism to BChl 3 and further confirms the mainly dissipative nature of the energy transport mechanism involving this pathway, as demonstrated in Sec. V B.

We observe a remarkably strong positive correlation between  $\eta_4$  and  $L_{\rho,avg}$ , with a correlation coefficient of 0.90. We also examined the correlation with  $V_{34}$  set to zero in the system Hamiltonian, in order to address the concern that this correlation could be predominantly attributed to the strong coupling between BChls 3 and 4. While the positive correlation decreased as expected, it remains strong with a correlation coefficient of 0.76. This shows that even though the strong coupling between the two pigments undoubtedly plays a role, it is not overwhelmingly responsible for the correlation between delocalization/coherence and the efficiency measure,  $\eta_4$ , for this pathway.

Figure 3 also clearly showcases the capability of the FMO  $\lambda_m$  configuration to accommodate efficient energy transport to both target sites, as we have inferred in Secs. V A and V B. Even though the FMO  $\lambda_m$  configuration does not lead to the best efficiency for either of the target sites, it nevertheless corresponds to relatively high efficiency for both target

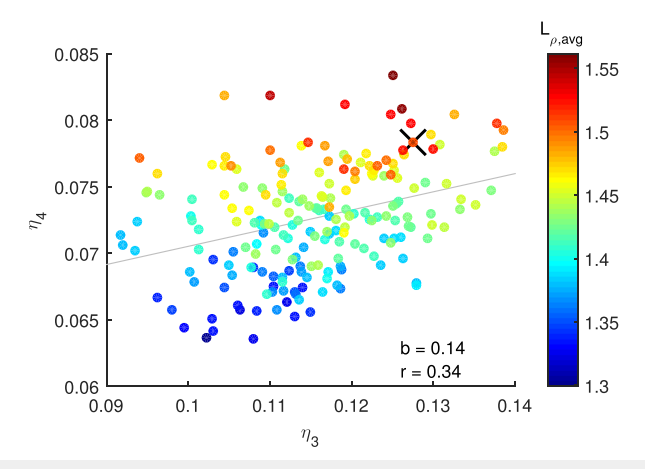


FIG. 4. Scatter plot using the same 206 data points from Fig. 3 showing the relation between the efficiencies  $\eta_3$  and  $\eta_4$  at the target sites of BChls 3 and 4, respectively. The black cross indicates the data point corresponding to the original configuration. Numerical method: CMRT.

sites. In contrast, two of the most optimized configurations,  $\lambda_{m,3}^{ga}$  ( $\lambda_{m,4}^{ga}$ ) and  $\lambda_{m,3}^{perm}$  ( $\lambda_{m,4}^{perm}$ ) only produce superior efficiencies for their respective target site BChl 3(4) but are significantly less remarkable and are even inferior to the FMO configuration for the other target site BChl 4(3). This illustrates the nontriviality of navigating trade-offs to sufficiently accommodate two largely uncorrelated and partially conflicting processes. The highly coherent nature of  $\lambda_{m,4}^{ga}$  and  $\lambda_{m,4}^{perm}$  (as reflected by their large  $L_{\rho,avg}$  values) while advantageous for the partially coherent energy transport to BChl 4, is unconstructive for the dissipative energy transport to BChl 3 (Fig. 3). Similarly,  $\lambda_{m,3}^{ga}$ and  $\lambda_{m,3}^{perm}$  which only correspond to moderate coherence only lead to average efficiencies at BChl 4 (Fig. 3). Meanwhile, the FMO  $\lambda_m$  configuration gives rise to a rather impressive degree of exciton delocalization, where its  $L_{\rho,avg}$  value lies between that of  $\lambda_{m,3}^{ga}$  ( $\lambda_{m,3}^{perm}$ ) and  $\lambda_{m,4}^{ga}$  ( $\lambda_{m,4}^{perm}$ ), resulting in intermediate  $\eta_3$  an  $\eta_4$  values.

Finally, we explore the question of independence between the observed optimization of  $\eta_3$  and  $\eta_4$ . This is an important point to address since the relatively strong coupling between BChls 3 and 4 raises the possibility that the optimization observed at one target site could simply be a side effect of optimization at the other target site. From the differences in energy transport mechanism and the somewhat different site distribution of  $\lambda_{m,3}^{ga}$  and  $\lambda_{m,4}^{ga}$  (Table II), it can be inferred that these two quantities are reasonably uncorrelated. This can be seen explicitly from Fig. 4 where we have recast the data, showing that the efficiencies are only weakly correlated.

#### VI. CONCLUSIONS

To summarize, we have proposed a plausible design principle for FMO that involves an effective interplay between the system and system-bath interaction. Energy transport mechanisms and pathways are combined with the fine-tuning of pigment-protein interaction in such a way that the (inevitable) site-varying system-bath interaction strengths are efficiently exploited to optimize energy transport. The optimization is observed not only for the commonly assigned target site of BChl 3 but also for BChl 4, a site which has not received as much attention as a target site despite some previous suggestions of its role. More importantly, this optimization for the two target sites is largely uncorrelated, meaning that the observed optimization at BChl 4 is non-trivial.

In fact, it appears that the electronic system itself may be designed to transport energy to the two target sites using two different mechanisms of energy transport. For BChl 3, the optimal mechanism is purely dissipative funnelling, while for BChl 4, the optimal mechanism is partially coherent. This implies that the system and system-bath interaction are configured in such a way that both dissipative and coherent processes are reasonably accommodated. Indeed, we observe an optimization of exciton delocalization when the FMO Hamiltonian is paired with the realistic configuration of site-dependent reorganization energies.

This simultaneous optimization of two largely uncorrelated processes of somewhat opposing nature is noteworthy since it suggests the presence of an underlying evolutionary design principle. It requires spatial "engineering" of systembath interaction such that the magnitude of the reorganization energies either mutually benefits energy transport to both target sites or at least does not negatively impact energy transport to any of the target sites too significantly. Hence, if the simultaneous optimization at the two target sites is not purely accidental, and if coherence does indeed play a role in the FMO complex, then the conventional view of BChl 3 as the sole linker site to the reaction centre is possibly incomplete.

#### **ACKNOWLEDGMENTS**

We thank Dr. Mi Kyung Lee and Associate Professor Kwek Leong Chuan for useful discussions. We are also grateful to Mi Kyung Lee for providing the spectral density data used in this work. S.A.O. and D.A.W.H. gratefully acknowledge financial support from the Dodd-Walls Centre for Photonic and Quantum Technologies. S.A.O. and D.A.W.H. also acknowledge the computational resources provided by the New Zealand eScience Infrastructure (NeSI). D.F.C. acknowledges financial support from US NSF (Grant No. CHE-1665367).

#### APPENDIX A: MODIFIED REDFIELD THEORY

The exciton population dynamics is described by the following rate equation:

$$\frac{dP(t)}{dt} = K^{MRT}P(t), \tag{A1}$$

where KMRT is the modified Redfield rate matrix and  $P(t) = [P_1(t) P_2(t) \dots P_k(t) \dots P_M(t)]^{\mathsf{T}}$  is a vector of exciton populations at time t, with the total number of exciton states M = N. The matrix element  $K_{k,k'}^{MRT}$  of  $K^{MRT}$  is the population transfer rate from the k'th to the kth exciton state and is given by the following time integral:

$$K_{k,k'}^{\text{MRT}} = 2\text{Re} \int_0^\infty d\tau F_{k'}^*(\tau) A_k(\tau) N_{k,k'}(\tau),$$
 (A2)

where

$$\begin{split} F_{k'}(\tau) &= \exp(-i(E^0_{k'} - \lambda_{k'})\tau - g^*_{k'k',k'k'}(\tau)), \\ A_k(\tau) &= \exp(-i(E^0_k + \lambda_k)\tau - g_{kk,kk}(\tau)), \\ N_{k,k'}(\tau) &= \left(\ddot{g}_{k'k,kk'}(\tau) - \left[\dot{g}_{k'k,kk}(\tau) - \dot{g}_{k'k,k'k'}(\tau) - 2i\lambda_{k'k,k'k'}\right]\right) \\ &\times \left[\dot{g}_{kk',kk}(\tau) - \dot{g}_{kk',k'k'}(\tau) - 2i\lambda_{kk',k'k'}\right] \\ &\times e^{2(g_{kk,k'k'}(\tau) + i\lambda_{kk,k'k}\tau)}. \end{split}$$

Here,  $\lambda_{\delta\sigma,\kappa\mu}$  and  $g_{\delta\sigma,\kappa\mu}(t)$  are the exciton counterparts of the site reorganization energy  $\lambda_m$  and site lineshape function  $g_m(t)$ , respectively, with the relationships expressed as

$$\lambda_{\delta\sigma,\kappa\mu} = \sum_{m=1}^{N} a_{\delta\sigma}(m) a_{\kappa\mu}(m) \lambda_m, \tag{A3}$$

$$g_{\delta\sigma,\kappa\mu}(t) = \sum_{m=1}^{N} a_{\delta\sigma}(m) a_{\kappa\mu}(m) g_m(t), \tag{A4}$$

where  $a_{k,k'}(m) = c_{m,k}^* c_{m,k'}$ .  $\lambda_k = \lambda_{kk,kk}$  is the kth exciton reorganization energy, which when subtracted from the kth exciton transition energy  $E_k$  (i.e., the kth eigenenergy of  $H_s$ ), gives the corresponding 0-0 transition energy, i.e.,  $E_k^0 = E_k - \lambda_k$ . Meanwhile, the site lineshape function  $q_m(t)$  is defined by the following double time integral:

$$g_m(t) = \int_0^t dt_1 \int_0^{t_1} dt_2 C_m(t_2),$$
 (A5)

where  $C_m(t)$  is the complex bath correlation function which can be written as

$$C_m(t) = \frac{1}{\pi} \int_0^\infty d\omega J_m(\omega) \Big[ \cos(\omega t) \coth\left(\frac{\beta \omega}{2}\right) - i \sin(\omega t) \Big]. \quad (A6)$$

Thus,  $g_m(t)$  can be computed from the spectral density  $J_m(\omega)$ from the following relation:

$$g_m(t) = \frac{1}{\pi} \int_0^\infty d\omega \frac{J_m(\omega)}{\omega^2} \left[ (1 - \cos \omega t) \coth\left(\frac{\beta \omega}{2}\right) + i(\sin \omega t - \omega t) \right]. \tag{A7}$$

The integrand in Eq. (A7) contains poles, and thus the lower limit of integration must be changed to an appropriately small finite value for numerical integration. Alternatively, the poles can be removed at the level of C(t) by analytical means, such as in the case of the Drude-Lorentz representation. The derivation of the analytical form of  $g_m(t)$  for the Drude-Lorentz spectral density is shown in Appendix D.

Finally, the diagonal elements of K<sup>MRT</sup> are computed from

$$K_{k,k}^{\text{MRT}} = -\sum_{k'} K_{k',k}^{\text{MRT}}.$$
 (A8)

Equation (A1) can then be easily solved with P(t) $=e^{K^{MRT}t}P(0)$ . Here the initial population vector consists of the exciton populations corresponding to the initial excitation site  $m_0$ , i.e.,  $P(0) = [c_{m_0,1}^2 c_{m_0,2}^2 \dots c_{m_0,k}^2 \dots c_{m_0,M}^2]^{\mathsf{T}}$ . It should be pointed out that the numerical integration in

Eq. (A2) requires a finite cutoff value for the upper integration

limit. In general, the stronger the system-bath coupling, the more oscillatory the integrand and the longer it takes for the integrand function to taper off. We have taken care to ensure our chosen cutoff value of  $\tau$  = 1 ps is acceptable by checking that increasing the cutoff has negligible effect on the calculated rates. For the genetic algorithm and statistical evaluation performed in this work, such manual inspection would be impractical. As such, we have applied a "worst case scenario" test by assigning  $\lambda_m$  with the largest reorganization energy to each site and confirmed that there is no appreciable change in the computed rates when the value of the cutoff is increased to 5  $ps^{-1}$ .

#### APPENDIX B: COHERENT MODIFIED REDFIELD THEORY

The formula for the exciton transfer rates for CMRT is similar to Eq. (A2), except with the upper limit of integration replaced by t to incorporate non-Markovianity. That is, the rates are time-dependent in contrast to the Markovian MRT case. We shall denote this exciton population transfer rate (from exciton k' to k) as  $K_{k,k'}^{\text{CMRT}}(t)$ . Due to the inclusion of coherences in CMRT, dephasing rates must also be accounted for and is defined by the following relation:

$$L_{kk'}(t) = \sum_{m} \left[ a_{kk}(m) - a_{k'k'}(m) \right]^2 \text{Re} \left[ \dot{g}_m(t) \right].$$
 (B1)

It turns out that the CMRT master equation can be cast into a generalized Lindblad form

$$\frac{d\rho(t)}{dt} = -i \left[ \hat{H_e}, \rho(t) \right] - \frac{1}{2} \sum_{k,k'} R_{kk'}(t) \left[ \left\{ A_{kk'}^{\dagger} A_{kk'}, \rho(t) \right\} - 2 A_{kk'} \rho(t) A_{kk'}^{\dagger} \right]. \tag{B2}$$

This allows the master equation to be conveniently solved using the Non-Markovian Quantum Jump (NMQJ) approach. The summary of the NMQJ technique is provided in Appendix C, while full details and derivation can be found in Refs. 20, 21, and 41. In Eq. (B2),  $A_{kk'} = |k\rangle\langle k'|$  are the jump operators, while  $H_e = \sum_k E_h^0 |k\rangle\langle k|$  is the modified system Hamiltonian that governs the coherent evolution. The jump rates  $R_{kk'}(t)$  from exciton state k' to k are such that

$$R_{kk'}(t) = \begin{cases} G_k(t) & \text{for } k = k', \\ K_{bb'}^{CMRT}(t) & \text{for } k \neq k', \end{cases}$$
(B3)

where  $G_k(t)$  is the kth element of vector G(t) which is linked to the pure dephasing rate  $L_{kk'}(t)$ . This relation is given by  $G(t) = B^{-1}D(t)$ , where B is a matrix and D(t) is a time-dependent vector whose elements are defined, respectively, as

$$B_{kk'} = \begin{cases} 0.5 & \text{for } k' < k, \\ 0.5(2M - k') & \text{for } k = k', \\ 1 & \text{for } k < k' < M, \\ 0.5 & \text{otherwise,} \end{cases}$$
(B4)

$$D_a(t) = \sum_{k=a+1}^{M} L_{ak}(t) + \sum_{k=1}^{M-1} L_{ka}(t).$$
 (B5)

#### APPENDIX C: NON-MARKOVIAN QUANTUM JUMP

The Non-Markovian Quantum Jump (NMQJ) is a tool for the stochastic unravelling of a non-Markovian quantum master equation and is the non-Markovian generalization of the well-known Monte Carlo Wave Function (MCWF) method. 42.43 It takes advantage of the general definition of the density matrix,

$$\rho(t) = \sum_{\alpha} \frac{N_{\alpha}(t)}{N} |\psi_{\alpha}(t)\rangle \langle \psi_{\alpha}(t)|, \tag{C1}$$

where N is the ensemble size and  $N_{\alpha}$  is the number of ensemble members in the state  $|\psi_{\alpha}(t)\rangle$  and operates on the level of the state vector

In this work, the  $|\psi_{\alpha}(t)\rangle$ s are the exciton states  $|k\rangle$  and the time-evolved initial state  $|\psi_{0}(t)\rangle$ .  $|\psi_{0}(t)\rangle$  is a coherent superposition of exciton states in which  $|\psi_{0}(0)\rangle = |m_{0}\rangle$ , where  $|m_{0}\rangle$  is the initial localized site basis. Due to the construct of the density matrix, the single exciton states are time-independent as global phases are cancelled out. Hence Eq. (C1) can be rewritten as

$$\rho(t) = \frac{N_0(t)}{N} |\psi_0(t)\rangle\langle\psi_0(t)| + \sum_k \frac{N_k(t)}{N} |k\rangle\langle k|.$$
 (C2)

Note that  $\rho(t)$  is in the site basis due to Eq. (3).

According to the NMQJ formulation, each ensemble member undergoes continuous time evolution interrupted by discontinuous probabilistic jumps. The propagation of the state vector proceeds in small time steps  $\delta t$  with the deterministic evolution described by

$$|\psi_{\alpha}(t+\delta t)\rangle = \frac{e^{-i\hat{H}_{eff}^{-}\delta t}|\psi_{\alpha}(t)\rangle}{\left\|e^{-i\hat{H}_{eff}^{-}\delta t}|\psi_{\alpha}(t)\rangle\right\|},\tag{C3}$$

where the effective non-Hermitian Hamiltonian is defined as

$$\hat{H}_{eff}(t) = \hat{H}_e - \frac{i}{2} \sum_{k k'} R_{kk'}(t) A_{kk'}^{\dagger} A_{kk'}.$$
 (C4)

When  $R_{kk'}(t) \geq 0$ , an instantaneous positive jump to another state  $|\psi_{\alpha'}(t)\rangle$  may occur, and the state at the next time step would be set to this new state

$$|\psi_{\alpha}(t)\rangle \to \frac{A_{kk'}|\psi_{\alpha}(t)\rangle}{\|A_{kk'}|\psi_{\alpha}(t)\rangle\|} = |\psi_{\alpha'}(t+\delta t)\rangle. \tag{C5}$$

Here the probability of the jump occurring through the channel  $k' \to k$  for a given ensemble member state  $|\psi_{\alpha}\rangle$  is

$$P_{\alpha,kk'}^{\dagger}(t) = R_{kk'}(t)\delta t \langle \psi_{\alpha}(t)|A_{kk'}^{\dagger}A_{kk'}|\psi_{\alpha}(t)\rangle. \tag{C6}$$

Unlike purely Markovian dynamics, the non-Markovian transition rate  $R_{kk'}(t)$  is time-dependent and can become negative. During this time period, the action of the positive jump

operator  $A_{kk'}$  is to bring the target state  $|\psi_{\alpha'}(t)\rangle$  to the source state  $|\psi_{\alpha}(t)\rangle$ ,

$$|\psi_{\alpha'}(t+\delta t)\rangle \leftarrow |\psi_{\alpha}(t)\rangle = \frac{A_{kk'}|\psi_{\alpha'}(t)\rangle}{|A_{kk'}|\psi_{\alpha'}(t)\rangle|}.$$
 (C7)

This implies that the negative jump operator  $A^-_{kk'} = |\psi_{\alpha'}(t)\rangle\langle\psi_{\alpha}(t)|$ . In other words, a negative jump means the reversal of a previous jump back to a prior state. The probability for a reverse jump is given by

$$P_{\alpha \to \alpha',kk'}^{-}(t) = \frac{N_{\alpha'}(t)}{N_{\alpha}(t)} |R_{kk'}(t)| \delta t \langle \psi_{\alpha'}(t) | A_{kk'}^{\dagger} A_{kk'} | \psi_{\alpha'}(t) \rangle. \tag{C8}$$

With each jump, the number of ensemble members in the source and target states are updated accordingly for the current time step, i.e.,  $N_{\alpha}(t) - 1$  and  $N_{\alpha'}(t) + 1$ , respectively.

The choice between deterministic evolution and jump is determined by a random number  $0 < \epsilon < 1$ . If  $\epsilon$  is less than or equal to the total jump probabilities of all channels, a jump occurs and vice versa. If a jump is determined, another random number s is generated to randomly select the jump channel.

At t=0, all the ensemble members are in  $|\psi_0(0)\rangle$ , i.e.,  $N_0(0)=N$ . This means that the propagation of the density matrix starts from a pure state and progresses to a mixed state through positive jumps. At a later time when the rates become negative, negative jumps can undo these positive jumps, and this may include the revival of coherences via a reverse jump to  $|\psi_0(t)\rangle$ . For FMO, there are 56 relaxation and 8 dephasing channels. As can be seen from Eq. (C2), efficient computation and averaging of the constituent density matrices can be achieved by simply updating  $N_{\alpha}(t)$  and  $N_{\alpha'}(t)$  at each time step and performing a one-off time evolution of  $|\psi_0(t)\rangle$ .

## APPENDIX D: ANALYTICAL FORM OF THE DRUDE-LORENTZ LINESHAPE FUNCTION

Since the Drude-Lorentz spectral density  $J_m^{\rm DL}(w)$  has simple poles at  $\omega=\pm i\Omega_m$ , the residue theorem can be conveniently applied to obtain the analytical form of the bath correlation function  $C_m(t)^{4.4}$  which is

$$C_m(t) = \sum_{k=1}^{n_r} \alpha_k^r e^{\gamma_k^r t} - i\alpha^i e^{\gamma^i t},$$
 (D1)

where

$$\alpha_{k}^{r} = \begin{cases} \lambda_{m} \Omega_{m} \cot\left(\frac{\beta \Omega_{m}}{2}\right) & \text{for } k = 1, \\ \\ -\frac{4\lambda_{m}}{\beta \Omega_{m}} \frac{\nu_{k-1}}{1 - (\nu_{k-1}/\Omega_{m})^{2}} & \text{for } k = 2 \text{ to } n_{r}, \end{cases}$$

$$\gamma_k^r = \begin{cases} -\Omega_m & \text{for } k = 1, \\ \\ -\nu_{k-1} & \text{for } k = 2 \text{ to } n_r, \end{cases}$$

$$\alpha^i = \lambda_m \Omega_m,$$
$$\gamma^i = -\Omega_m.$$

Here  $\nu_k=\frac{2\pi k}{\beta}$  are the Matsubara frequencies. In principle, the Matsubara expansion is infinite but in practice, the summation can be truncated at some finite value  $n_r$ . The number of terms required for convergence is dependent only on temperature, with more terms needed for lower temperatures.

Substituting into Eq. (A5), we arrive at the analytical form of the lineshape function

$$g_m(t) = \sum_{k=1}^{n_r} \frac{\alpha_k^r}{(\gamma_k^r)^2} (e^{\gamma_k^r t} - \gamma_k^r t - 1) - i \frac{\alpha^i}{(\gamma^i)^2} (e^{\gamma^i t} - \gamma^i t - 1).$$
 (D2)

## APPENDIX E: HISTOGRAM OF EFFICIENCIES FOR RANDOM CONFIGURATIONS OF $\lambda_m$

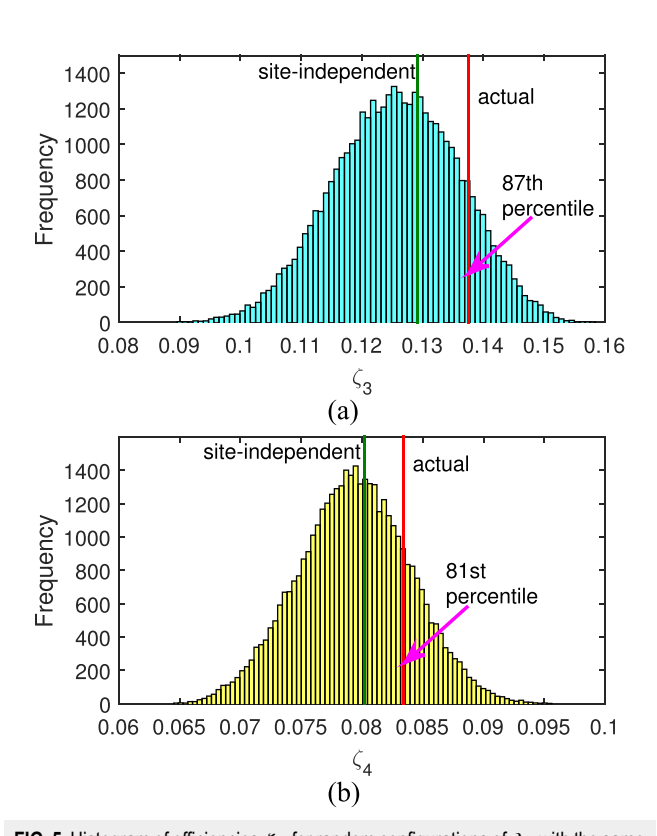


**FIG. 5.** Histogram of efficiencies  $\zeta_m$  for random configurations of  $\lambda_m$  with the same mean, maximum, and minimum as the original for the exciton state (corresponding target site) of (a)  $\alpha$  = 1 (BChl 3) and (b)  $\alpha$  = 2 (BChl 4). In both histograms, the original configuration is also included in the sample and the sample size is the same as in Fig. 1, i.e., 40 320. The red and green vertical lines indicate the position on the histogram of the original and site-independent configurations, respectively. Numerical method: MRT.

## APPENDIX F: NUMERICAL DETAILS OF THE GENETIC ALGORITHM

We have utilized the genetic algorithm solver from the MATLAB optimization toolbox with the following parameters: (i) population size: 80; (ii) selection function: stochastic uniform; (iii) elite count: 4; (iv) crossover function: intermediate; (v) crossover fraction: 0.8; (vi) mutation function = adaptive feasible; and (vii) number of generations: 4000. To maximize the efficiency of the algorithm while representing a realistic scenario at the same time, we confined the search space to be within the minimum and maximum values of the original  $\lambda_m$ . The choice of the upper bound is also important for another reason: in order for a positive correlation between larger  $\lambda_m$  and higher efficiency to stay valid for a dissipative process, the allowed values of  $\lambda_m$  must not be so large to the point that transport is suppressed due to localization.

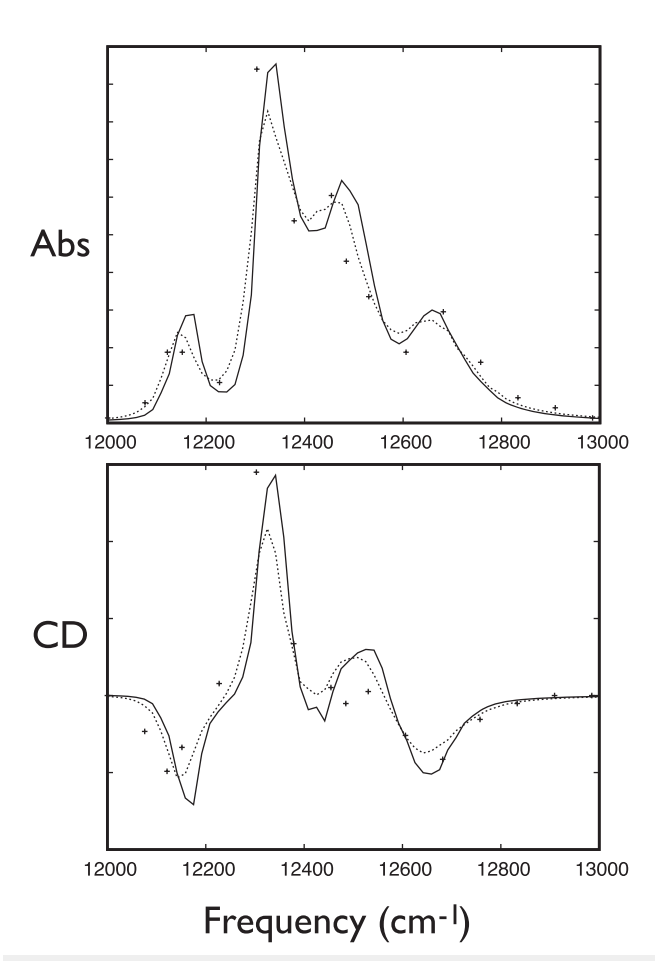


**FIG. 6.** Comparison of 8 state FMO model absorption and CD spectra computed with site-dependent (solid) and site-independent (dotted) super-Ohmic Renger model spectral densities and Gaussian sampling of inhomogeneous linewidths. 26,46 Experimental results are also presented (+symbols). Results are for T = 77 K.

## APPENDIX G: INFLUENCE OF SITE-DEPENDENT SPECTRAL DENSITIES ON ABSORPTION AND CD SPECTRA

Figure 6 explores the influence of the site dependence of individual chromophore spectral densities on linear spectroscopic properties. In this study, the absorption and circular dichroism (CD) spectra were first computed<sup>45</sup> using the model of Renger and co-workers<sup>26,46</sup> which assumes all chromophores have the identical fitted spectral densities. The "super-Ohmic" form of this spectral density is particularly well formulated for computation of spectroscopic properties as its rapid fall off at low frequencies gives spectra that show weak variation with temperature as observed experimentally.<sup>47</sup> The Drude-Lorentz truncated Ohmic form used in the energy transport efficiency studies reported in the paper, while convenient for dynamical calculations employed in these studies, gives accurate spectra at low temperatures but this form gives spectra that broaden too quickly as the temperature is increased. In Fig. 6, the spectra computed with this site-independent model of Renger and co-workers (dotted curves) are compared with results from a site-dependent

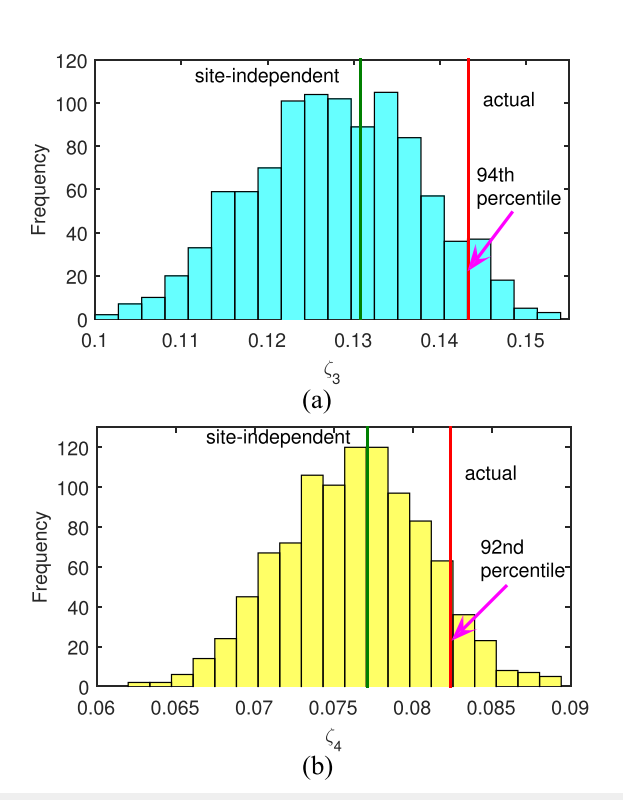


**FIG. 7.** Histogram of efficiency  $\zeta_m$  for random configurations of  $\lambda_m$  similar to those presented in Fig. 5, only now the super-Ohmic Renger model spectral density<sup>26,46</sup> and a sample size of 1001 (which includes the original  $\lambda_m$  configuration) are employed. The smaller sample size is chosen to accommodate the longer computation time since the lineshape function  $g_m(t)$  is computed numerically. Nevertheless, this sample size should be sufficiently large for statistical accuracy.

model (solid curves) obtained by simply scaling these spectral densities so that each chromophore's site dependent reorganization energy is the same as the previously computed values<sup>2</sup> summarized in the second column of Table I. We see that employing a site-dependent model does give a small variation in the computed linear spectroscopic properties, and comparison with experimental spectra (+symbols) suggests that, while these differences are small, there is an enhancement in the ability of the site-dependent model to capture different relative peak magnitudes and widths. The Renger model we used here also includes different inhomogeneous broadening contributions for the various sites as adjustable parameters. These calculated spectra are averaged over 300 realizations of the static site energy disorder. These inhomogeneous distributions can be computed from first principles<sup>48</sup> and a clearer understanding of the importance of site-dependent spectral density variability could be obtained by fixing some of these adjustable parameters.

Finally, in Fig. 7 we present histograms of our energy transport efficiency measures to target sites BChls 3 and 4. These results are also obtained using the site-dependent super-Ohmic Renger model spectral densities outlined above. These results suggest that the actual calculated site dependent model reorganization energies give robust enhancement of energy transport efficiency that is fairly independent of the form of the spectral density.

#### **REFERENCES**

- <sup>1</sup>M. K. Lee and D. F. Coker, J. Phys. Chem. Lett. 7, 3171 (2016).
- <sup>2</sup>E. Rivera, D. Montemayor, M. Masia, and D. F. Coker, J. Phys. Chem. B **117**, 5510 (2013).
- <sup>3</sup>C. Olbrich, J. Strümpfer, K. Schulten, and U. Kleinekathöfer, J. Phys. Chem. Lett. 2, 1771 (2011).
- <sup>4</sup>Y. Sato and M. F. Reynolds, J. Phys. Chem. B **118**, 1229 (2014).
- <sup>5</sup>M. Mohseni, P. Rebentrost, S. Lloyd, and A. Aspuru-Guzik, J. Chem. Phys. 129, 174106 (2008).
- <sup>6</sup>M. B. Plenio and S. F. Huelga, New J. Phys. 10, 113019 (2008).
- <sup>7</sup>A. Ishizaki and G. R. Fleming, Proc. Natl. Acad. Sci. U. S. A. **106**, 17255 (2009).
- <sup>8</sup>P. Rebentrost, M. Mohseni, I. Kassal, S. Lloyd, and A. Aspuru-Guzik, New J. Phys. **11**, 033003 (2009).
- <sup>9</sup>F. Caruso, A. W. Chin, A. Datta, S. F. Huelga, and M. B. Plenio, J. Chem. Phys. **131**, 105106 (2009).
- <sup>10</sup> A. W. Chin, A. Datta, F. Caruso, S. F. Huelga, and M. B. Plenio, New J. Phys. 12, 065002 (2010).
- <sup>11</sup>M. K. Lee, P. Huo, and D. F. Coker, Annu. Rev. Phys. Chem. **67**, 639 (2016).
- <sup>12</sup>S. A. Oh, D. F. Coker, and D. A. W. Hutchinson (unpublished).
- <sup>13</sup>J. M. Moix, J. Wu, P. Huo, D. F. Coker, and J. Cao, J. Phys. Chem. Lett. 2, 3045 (2011).
- <sup>14</sup>W. M. Zhang, T. Meier, V. Chernyak, and S. Mukamel, J. Chem. Phys. **108**, 7763 (1998).
- 15 Y.-H. Hwang-Fu, W. Chen, and Y.-C. Cheng, Chem. Phys. 447, 46 (2015).
- <sup>16</sup>Y. Chang and Y.-C. Cheng, J. Chem. Phys. 142, 034109 (2015).
- <sup>17</sup>Q. Ai, Y.-J. Fan, B.-Y. Jin, and Y.-C. Cheng, New J. Phys. **16**, 053033 (2014).
- <sup>18</sup>M.-J. Tao, Q. Ai, F.-G. Deng, and Y.-C. Cheng, Sci. Rep. **6**, 27535 (2016).
- <sup>19</sup>M. Yang and G. R. Fleming, Chem. Phys. 282, 163 (2002).
- <sup>20</sup>J. Piilo, S. Maniscalco, K. Härkönen, and K.-A. Suominen, Phys. Rev. Lett. 100, 180402 (2008).
- <sup>21</sup>J. Piilo, K. Härkönen, S. Maniscalco, and K.-A. Suominen, Phys. Rev. A 79, 062112 (2009).

- <sup>22</sup>M. Schmidt am Busch, F. Müh, M. El-Amine Madjet, and T. Renger, J. Phys. Chem. Lett. 2, 93 (2010).
- <sup>23</sup>A. Ben-Shem, F. Frolow, and N. Nelson, FEBS Lett. **564**, 274 (2004).
- <sup>24</sup>D. E. Tronrud, J. Wen, L. Gay, and R. E. Blankenship, Photosynth. Res. **100**, 79 (2009).
- <sup>25</sup>J. Wen, H. Zhang, M. L. Gross, and R. E. Blankenship, Proc. Natl. Acad. Sci. U. S. A. **106**, 6134 (2009).
- <sup>26</sup>J. Adolphs and T. Renger, Biophys. J. **91**, 2778 (2006).
- <sup>27</sup>G. Ritschel, J. Roden, W. T. Strunz, A. Aspuru-Guzik, and A. Eisfeld, J. Phys. Chem. Lett. 2, 2912 (2011).
- <sup>28</sup>J. Zhu, S. Kais, P. Rebentrost, and A. Aspuru-Guzik, J. Phys. Chem. B **115**, 1531 (2011).
- <sup>29</sup>Y.-C. Cheng and G. R. Fleming, Annu. Rev. Phys. Chem. **60**, 241 (2009).
- <sup>30</sup>A. Shabani, M. Mohseni, H. Rabitz, and S. Lloyd, Phys. Rev. E **89**, 042706 (2014).
- <sup>31</sup>S. Mukamel, Principles of Nonlinear Optical Spectroscopy (Oxford University Press, New York, 1995).
- <sup>32</sup> J. Wu, F. Liu, Y. Shen, J. Cao, and R. J. Silbey, New J. Phys. **12**, 105012 (2010).
- 33 Y. Sato and B. Doolittle, J. Chem. Phys. 141, 185102 (2014).

- 34 M. H. Lee and A. Troisi, J. Chem. Phys. 146, 075101 (2017).
- $^{\bf 35}{\rm E.~J.}$  O'Reilly and A. Olaya-Castro, Nat. Commun. 5, 3012 (2014).
- <sup>36</sup>P. Rebentrost, R. Chakraborty, and A. Aspuru-Guzik, J. Chem. Phys. 131, 184102 (2009).
- <sup>37</sup>N. Renaud, M. A. Ratner, and V. Mujica, J. Chem. Phys. **135**, 075102 (2011).
- <sup>38</sup>T. Meier, V. Chernyak, and S. Mukamel, J. Phys. Chem. B **101**, 7332 (1997).
- <sup>39</sup> M. Dahlbom, T. Pullerits, S. Mukamel, and V. Sundström, J. Phys. Chem. B **105**, 5515 (2001).
- <sup>40</sup>J. M. Moix, Y. Zhao, and J. Cao, Phys. Rev. B **85**, 115412 (2012).
- <sup>41</sup>H.-P. Breuer and J. Piilo, Europhys. Lett. **85**, 50004 (2009).
- <sup>42</sup>J. Dalibard, Y. Castin, and K. Mølmer, Phys. Rev. Lett. **68**, 580 (1992).
- <sup>43</sup>K. Mølmer, Y. Castin, and J. Dalibard, J. Opt. Soc. Am. B **10**, 524 (1993).
- 44 U. Kleinekathöfer, J. Chem. Phys. 121, 2505 (2004).
- 45 T. Renger and R. A. Marcus, J. Chem. Phys. 116, 9997 (2002).
- <sup>46</sup>J. Adolphs, F. Müh, M. E. Madjet, and T. Renger, Photosynth. Res. **95**, 197 (2008).
- <sup>47</sup>M. Wendling, M. A. Przyjalgowski, D. Gülen, S. I. E. Vulto, T. J. Aartsma, R. van Grondelle, and H. van Amerongen, Photosynth. Res. **71**, 99 (2002).
- <sup>48</sup>M. K. Lee, K. Bravaya, and D. F. Coker, J. Am. Chem. Soc. 139, 7803 (2017).